Modeling and Control of a PEM Fuel Cell System: A practical study based on experimental defined component behavior

Markus Özbek, Shen Wang, Matthias Marx, Dirk Söffker*

Chair of Dynamics and Control, SRS, University of Duisburg-Essen, Lotharstrasse 1-21, 47057 Duisburg, Germany

Abstract

In this contribution, the dynamical behavior of a polymer electrolyte membrane (PEM) fuel cell system is modeled; related control approaches are developed. The system model used for experimental and modeling purposes describes a 1.2 kW PEM fuel cell stack and an air blower. Due to the dynamical fuel cell - blower interaction the fuel cell stack and the blower model are validated to real systems respectively. Additionally, a feedback based on PI-control is used for hydrogen pressure control with an anode inlet valve. This controller is able to eliminate a stationary error between the anode and cathode pressures. For principal investigations three control approaches, a classical static feed-forward control approach, a state-space feedback control, and a novel gain-scheduling approach are developed, applied, and compared. As result, it can be shown that the feed-forward approach lacks in performance recovering the excess oxygen ratio to the desired level. The state-space feedback control shows stationary error. The introduced gain-scheduling con-

*Corresponding author. Tel.: +49 203 379-3429
Email address: soeffker@uni-due.de (Dirk Söffker)

trol approach leads to a fast excess oxygen ratio recovery without stationary deviations.
Key words: Polymer electrolyte membrane fuel cell, Dynamic modeling, Air supply system, Airflow management, Control, State feedback, Gain-scheduling

---

Constants

Symbol	Parameter	Unit	Value
b_{cm}	Blower motor constant	[Nms/rad]	2.3e-4
d_c	Blower diameter	[m]	0.0508
$k_{st}A_{st}$	Product between thermal conductivity and conducting surface area of stack	[J/K]	6.0
k_{cm}	Blower motor constant	[Nm/A]	0.089
k_v	Blower motor constant	[Vs/rad]	0.0752
$m_{st}C_{p,st}$	Product between mass and specific heat capacity of stack	[J/K]	2e4
m_{veh}	Vehicle total mass	[kg]	201.3
n_{fc}	Number of fuel cells	[-]	45
p_{amb}	Ambient pressure	[Pa]	101325
p_{cp}	Blower pressure	[Pa]	101325
t_m	Membrane thickness	[cm]	3e-3
A_{fc}	Fuel cell active area	[cm^2]	50
A_{veh}	Vehicle front area	[m^2]	0.83
C_d	Vehicle drag coefficient	[-]	0.37
γ	Ratio of specific heats of air	[-]	1.4

1. Introduction

Control of fuel cells is a demanding task due to the nonlinearity of the components as well as the overall system behavior. A proper control increases the fuel cell system efficiency and decreases the risk of oxygen starvation [1]. In [2] a comparison of control concepts is given. The approaches of static and dynamic feed-forward and full state feedback are based on linearized models of the fuel cell system. It can be concluded from these works that full state-feedback control shows better results than static and dynamic feed-forward with respect to oxygen starvation. However, nonlinear approaches are not tested yet. In [3], a related dynamic feed-forward control approach is introduced showing better results than static feed-forward approach used for comparison. Also here, the controller is developed based on a linearized model at a single nominal working point. Some papers introduce nonlinear approaches such as exact feedback linearization [4] and flatness-based control [5]. In principle, the feedback linearization method is developed on a simplified fuel cell model and shows lack of robustness towards modeling errors due to the simplification resulting from the control-oriented modeling. Applying feedback linearization on a detailed fuel cell model increases the complexity significantly. Flatness-based control [6] shows better results than feed-forward oriented ones. Due to their complexity these approaches are not applied on analytical fuel cell models. Gain-scheduled state feedback should decrease the complexity of dealing with nonlinearities due to the linearization of the model in several working points. This may allow to combine the simplicity of developing a controller based on a linear system together with advantages of increased performance known from nonlinear controllers. A

review of gain-scheduling approaches is given in [7], but has not yet been implemented on fuel cells.

This paper is organized as follows: in Section 2 the modeling of the fuel cell system including voltage and blower model will be explained. In Section 3, the control approaches will be implemented to the system model and compared to each other. The related simulation results are presented in Section 4. Finally, summary and outlook will be given in Section 5.

2. Fuel cell system: Modeling and experimental validation

In this section, the component models of the stack and air supply system will be introduced and validated to real system components. The fuel cell system with its corresponding fuel cell stack is depicted in Fig. 1. The fuel cell stack is manufactured and assembled at the Center for Fuel Cell Technology (ZBT GmbH) in Duisburg [8]. It consists of 45 cells and shows a rated voltage of 22 V at an output maximum power of 1.2 kW. Its working temperature is approximately 70 C and due to its water-cooling concept it has a higher power density than air-cooled fuel cell stacks. The control concepts developed here are implemented on this system. The development is based on the corresponding models.

2.1. PEM fuel cell stack model

The fuel cell stack is the core component of the considered fuel cell system. The electrochemical reaction

$$2H_2 + O_2 \rightleftharpoons 2H_2O \tag{1}$$

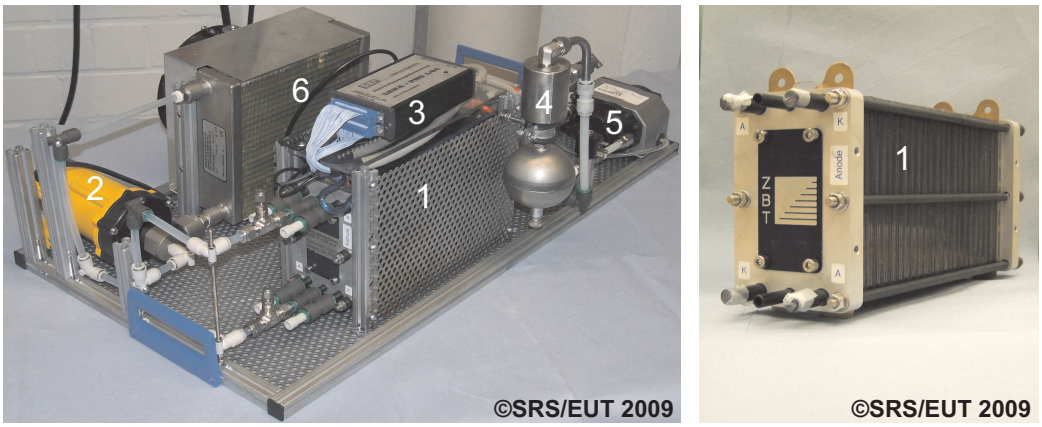

Figure 1: Left: Fuel cell system including peripheral components. Right: Fuel cell stack. 1. Fuel cell stack, 2. Cooling water pump, 3. Single cell voltage measurement, 4. Humidifier, 5. Hydrogen recycling pump, 6. Cooler

occurs inside the stack, where the reactants (hydrogen and oxygen) are fed to the anode and cathode side of the fuel cell stack respectively. The input to the stack model is the stack current i_{st} and the output is the stack voltage v_{st}. A fuel cell stack model usually consists of four submodels: the stack voltage model, the anode mass flow model, the cathode mass flow model, and the membrane hydration model. More details are given in [2]. Here, the equations of the stack voltage are briefly repeated. The stack voltage is given by

$$v_{st} = n_{fc} v_{fc}, \tag{2}$$

where n_{fc} denotes the number of cells and v_{fc} represents the single cell voltage, which is calculated as

$$v_{fc} = E_{o,fc} - v_{loss}, \tag{3}$$

where $E_{o,fc}$ denotes the open circuit voltage and v_{loss} the total voltage losses, i.e. activation, ohmic, and concentration losses. The voltage $E_{o,fc}$ can be calculated according to the Nernst equation by

$$\begin{aligned} E_{o,fc} &= 1.229 - 8.5 \times 10^{-4}(T_{fc} - 298.15) + \\ &\quad + 4.308 \times 10^{-5} T_{fc} \left(\ln\left(\frac{p_{H_2}}{101325}\right) + \frac{1}{2} \ln\left(\frac{p_{O_2}}{101325}\right) \right), \end{aligned} \tag{4}$$

where T_{fc} denotes the cell temperature, p_{H_2} the hydrogen partial pressure in the anode, and p_{O_2} the oxygen partial pressure in the cathode [9]. The voltage losses v_{loss} are described by

$$v_{loss} = v_{act} + v_{ohm} + v_{conc}, \tag{5}$$

where v_{act} is the voltage drop caused by activation losses, v_{ohm} denotes the ohmic losses, and v_{conc} the concentration losses. The activation losses v_{act} are calculated as

$$v_{act} = v_0 + v_a \left(1 - e^{-c_i i}\right), \tag{6}$$

where the constants v_0, v_a, and c_i are taken from [2]. Here i denotes the current density defined by

$$i = \frac{i_{st}}{A_{fc}}, \tag{7}$$

where A_{fc} represents the cell active area. The ohmic losses v_{ohm} are calculated as

$$v_{ohm} = i R_{ohm}, \tag{8}$$

where R_{ohm} denotes the internal electrical resistance and is related to the membrane conductivity σ_m by

$$R_{ohm} = \frac{t_m}{\sigma_m}, \tag{9}$$

where t_m denotes the membrane thickness. The membrane conductivity σ_m can be calculated as

$$\sigma_m = b_1 \exp\left(b_2\left(\frac{1}{303} - \frac{1}{T_{fc}}\right)\right), \tag{10}$$

where b_1 is related to the membrane water content λ_m and can be expressed with

$$b_1 = b_{11}\lambda_m - b_{12}. \tag{11}$$

The constants b_{11}, b_{12}, and b_2 for Nafion 117 membrane can be taken from [10]. The voltage drop due to the concentration losses is calculated as

$$v_{conc} = i\left(c_2\frac{i}{i_{max}}\right)^{c_3}, \tag{12}$$

where c_3 is a constant and i_{max} denotes the maximum current density. In [2], c_2 switches between two functions depending on the oxygen partial pressure and the water saturation pressure. However, while a low-pressure fuel cell system is considered, the variable c_2 is described as

$$\begin{aligned} c_2 = (7.16 \times 10^{-4} T_{fc} - 0.622)\left(\frac{p_{O_2}}{0.1173} + p_{sat}\right) - \\ - 1.45 \times 10^{-3} T_{fc} + 1.68. \end{aligned} \tag{13}$$

2.1.1. Experimental validation of the stack model

For validation of the electrical part, the fuel cell stack behavior is considered for a time range of 10 000 s. The mass flow rate of the air and hydrogen entering the stack, the corresponding pressures $p_{ca,in}$ and $p_{an,in}$, as well as the stack temperature T_{fc} are measured. The stack voltage of the real fuel cell stack v_{st} is the measured variable for the model validation to be compared to. The measured and simulated voltage for an arbitrary current load are depicted ink Fig. 2. During the warm-up of the fuel cell (0-1300 s) the stack voltage of the real fuel cell stack is not considered.

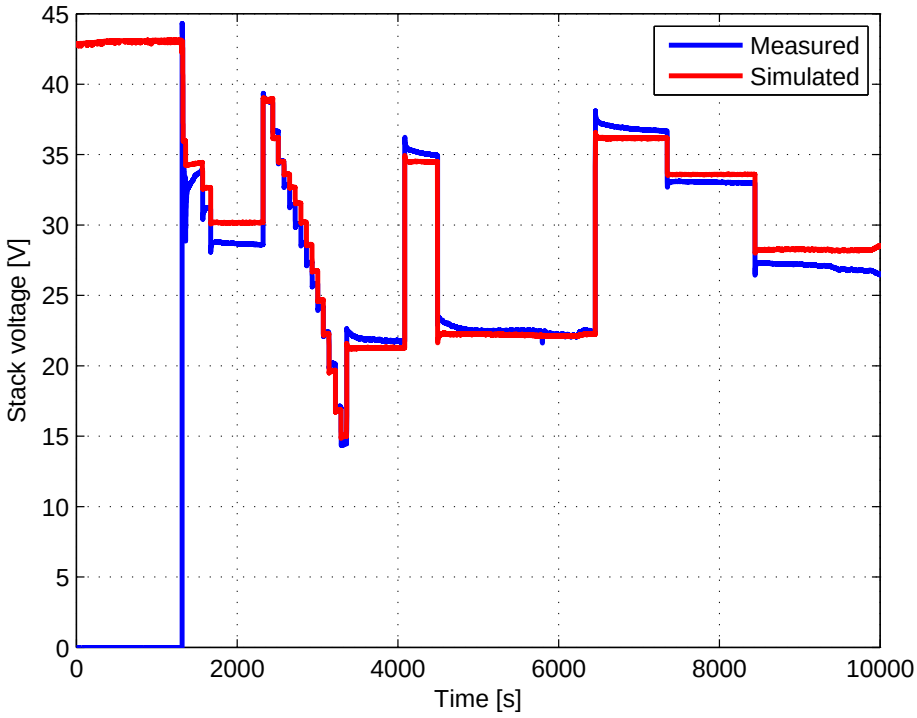

Figure 2: Validation of the electrical behavior by comparison of simulated and measured time behavior of a current input profile

2.2. Manifold model

The manifold model represents the connections (e. g. pipes etc.) between the fuel cell stack model and the air supply system model. Based on the relations described in [2] the physical properties of the air mass flow are calculated using the conservation principle

$$\frac{dm}{dt} = W_{in} - W_{out}, \tag{14}$$

with W_{in} and W_{out} denoting the flow rate at the input and the output of

the manifold and the ideal gas law stated by

$$\frac{dp}{dt} = \frac{\gamma R_a}{V}(W_{in}T_{in} - W_{out}T_{out}). \tag{15}$$

Hereby R_a denotes the gas constant of air, V the manifold volume, γ the ratio of specific heats of air and the temperature measurements at manifold input and output denoted as T_{in} and T_{out}. It should be noted that the model equations

2.3. Air supply system model

The modeling of the air supply system with the blower motor voltage v_{cm} as input and the outlet air flow $W_{cp,out}$ as output is introduced. The model of the blower is based on experimental results received from a real blower from a Nexa® power module fuel cell stack system from Ballard [11]. The blower model consists of two submodels as depicted in Fig. 3, the model of the blower motor and the blower map, which are developed in the sequel. For notation, the outlet pressure $p_{cp,out}$ corresponds to the fuel cell supply manifold pressure. The air supply system consists of a blower with a supply manifold that provides a mass flow of pressurized air to the fuel cell stack and of an electro-motor that drives the blower. Typical blower motors used in fuel cell applications are three-phase brushless DC-motors due to their high dynamics and high efficiency. The dynamical behavior of such motors is very similar to brushed DC-motors.

2.3.1. Blower motor

In [2] the motor driving the blower is simplified to its static behavior which is typical of large fuel cell systems (over 50 kW) with related large time

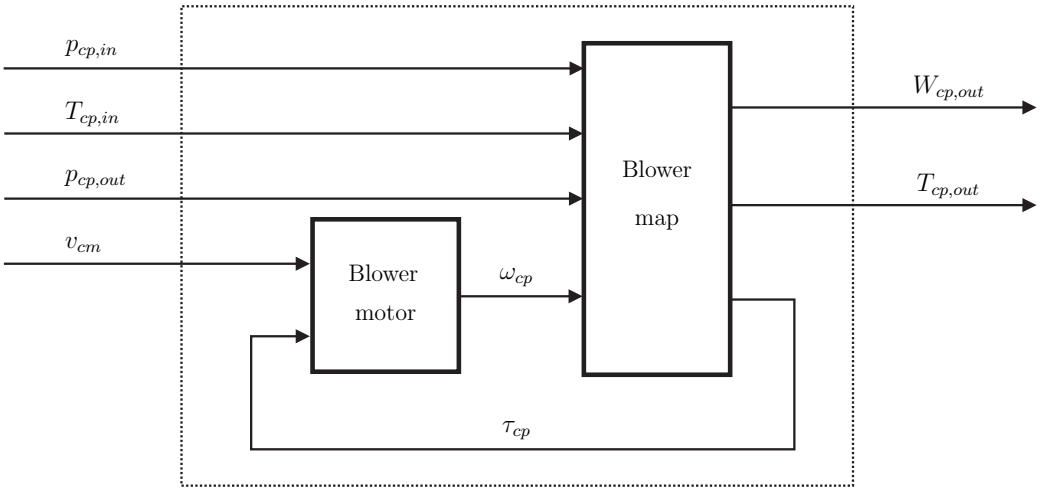

Figure 3: Block diagram of the blower model with corresponding inputs and outputs

constants. For smaller fuel cell systems (like the 1.2 kW system used here) the time constants are smaller, the bandwidth is higher, so the controller should provide the related behavior to realize the required dynamical behavior. By defining the dynamical behavior of the motor, the accuracy of the model increases and a suitable controller can be developed. The dynamical behavior of the blower speed is modeled by

$$J_{cp}\frac{d\omega_{cp}}{dt} = \tau_{cm} - \tau_f - \tau_{cp}, \tag{16}$$

where J_{cp} denotes the combined rotary inertia of the blower and the motor, τ_{cm} denotes the blower motor torque, τ_{cp} the external load on the motor, and τ_f denotes the torque loss in the motor due to damping and friction. The blower motor torque τ_{cm} can be calculated using the armature current i_{cm}

and a constant factor k_{cm} by

$$\tau_{cm} = k_{cm} i_{cm}. \tag{17}$$

The torque loss τ_f is assumed proportional to the blower speed by a constant factor b_{cm} with

$$\tau_f = b_{cm} \omega_{cp}. \tag{18}$$

The external load τ_{cp} is calculated in the blower map block. The dynamical behavior of the motor armature current is represented using Kirchhoff's voltage law by

$$L_{cm} \frac{di_{cm}}{dt} = v_{cm} - v_{R,cm} - v_{emf}, \tag{19}$$

where L_{cm} denotes the motor inductance, v_{cm} the input voltage to the blower motor, $v_{R,cm}$ the voltage drop over the internal electric resistance R_{cm}, and v_{emf} the induced voltage from the back electromotive force. The voltage drop over the resistance $v_{R,cm}$ is related to the armature current by

$$v_{R,cm} = R_{cm} i_{cm}. \tag{20}$$

2.3.2. Blower map

In the blower map as depicted in Fig. 3, the air mass flow from the blower $W_{cp,out}$, the temperature of the air leaving the blower $T_{cp,out}$, and the blower torque τ_{cp} are determined using static equations. The inputs to the blower map are the inlet $p_{cp,in}$ and outlet $p_{cp,out}$ air pressures, the blower speed ω_{cp}, as well as the air temperature entering the blower $T_{cp,in}$. The outlet manifold pressure $p_{cp,out}$ can either be calculated from the fuel cell model or inserted from measurements as it has been realized within this contribution. A typical approach determining the blower map is realized by including measurements

in look-up tables. However, the standard linear interpolation routines used in look-up tables are neither necessarily continuous nor differentiable so sometimes discontinuities may appear able to slow down simulations [12]. For this reason look-up tables are not well suited for usual control-oriented dynamic models. Instead, the measurement data of the blower performance can be represented by continuous functions, determined using nonlinear curve fitting methods. Such approaches used for modeling and their benefits are further mentioned in detail in [13]. As described in [12], the mass flow rate from the blower $W_{cp,out}$ is related to the corrected mass flow W_{cr} by

$$W_{cp,out} = W_{cr} \frac{p_{cr}}{\sqrt{T_{cr}}}, \tag{21}$$

where the corrected temperature is defined as $T_{cr} = T_{cp,in}/288$ and the corrected pressure as $p_{cr} = p_{cp,in}$. Corrected variables are applied in this model, because varying ambient conditions can be considered in the blower model[1]. The corrected mass flow W_{cr} is calculated as

$$W_{cr} = \Phi \rho_a \frac{\pi}{4} d_c^2 U_c, \tag{22}$$

where Φ denotes the normalized blower flow rate, ρ_a the air density, d_c the blower diameter, and U_c denotes the blower blade tip speed defined by

$$U_c = \frac{\pi}{60} d_c N_{cr}. \tag{23}$$

The corrected blower speed N_{cr} is related to the blower speed by

$$N_{cr} = \frac{60 \omega_{cp}}{2\pi \sqrt{T_{cr}}}. \tag{24}$$

[1]The corrected variables correspond to the values which would be measured at ambient conditions on a standard day at sea level, i.e. a temperature of 15°C and a pressure of 101 325 Pa

The normalized blower flow rate Φ can be expressed as a function of the head parameter Ψ by

$$\Phi = \frac{k_3 \Psi - k_1}{k_2 + \Psi}, \tag{25}$$

where k_i are factors which depend on the Mach number Ma of the inlet air and can be calculated as

$$k_i = a_i + b_i Ma, \quad i = 1, 2, 3, \tag{26}$$

where the Mach number Ma is defined by

$$Ma = \frac{U_c}{\sqrt{\gamma_a R_a T_{cp,in}}}. \tag{27}$$

The dimensionless head parameter Ψ is calculated using the method of Jensen & Kristensen as described in [13] with the relation

$$\Psi = \frac{C_{p,a} T_{cp,in} \left(\left(\frac{p_{cp,out}}{p_{cp,in}} \right)^{\frac{\gamma_a - 1}{\gamma_a}} - 1 \right)}{\frac{1}{2} U_c^2}, \tag{28}$$

where $C_{p,a}$ denotes the specific heat capacity and γ_a for the heat capacity ratio of air [14]. Another important blower performance parameter is the blower efficiency η_{cp}, which depends on the normalized mass flow rate Φ and the Mach number Ma and is expressed as

$$\eta_{cp} = c_1 \Phi^2 + c_2 \Phi + c_3, \text{ with} \tag{29}$$

$$c_i = \frac{d_i + e_i Ma}{f_i - Ma}, \quad i = 1, 2, 3. \tag{30}$$

The constants a_i, b_i, d_i, e_i, and f_i for $i = 1, 2, 3$ are parameters determined through curve fitting on the measurement data. The temperature of the air leaving the blower is given by

$$T_{cp,out} = T_{cp,in} + \Delta T_{cp}, \tag{31}$$

where ΔT_{cp} is the temperature change across the blower, which is calculated as

$$\Delta T_{cp} = \frac{\Delta h_{s,cp}}{C_{p,a}\eta_{cp}}, \tag{32}$$

where $\Delta h_{s,cp}$ denotes the isentropic enthalpy change across the blower and is calculated as

$$\Delta h_{s,cp} = \frac{\gamma_a}{\gamma_a - 1} R_a T_{cp,in} \left(\left(\frac{p_{cp,out}}{p_{cp,in}} \right)^{\frac{\gamma_a - 1}{\gamma_a}} - 1 \right). \tag{33}$$

According to Eqs. (31-33), it follows that the temperature $T_{cp,out}$ results to

$$T_{cp,out} = T_{cp,in} + \frac{\gamma_a}{\gamma_a - 1} \frac{R_a}{C_{p,a}} \frac{T_{cp,in}}{\eta_{cp}} \left(\left(\frac{p_{cp,out}}{p_{cp,in}} \right)^{\frac{\gamma_a - 1}{\gamma_a}} - 1 \right). \tag{34}$$

The relation between the heat capacity ratio γ_a and the gas constant of air is given by

$$\frac{R_a}{C_{p,a}} = \frac{\gamma_a - 1}{\gamma_a}. \tag{35}$$

Using this relation in (34) gives finally

$$T_{cp,out} = T_{cp,in} + \frac{T_{cp,in}}{\eta_{cp}} \left(\left(\frac{p_{cp,out}}{p_{cp,in}} \right)^{\frac{\gamma_a - 1}{\gamma_a}} - 1 \right). \tag{36}$$

The third output of the blower map, which is an input to the blower motor, is the blower torque τ_{cp}, which is calculated as

$$\tau_{cp} = \frac{P_{cp}}{\omega_{cp}}, \tag{37}$$

where the compressor power P_{cp} is defined by

$$P_{cp} = C_{p,a} W_{cp,out} \left(T_{cp,out} - T_{cp,in} \right). \tag{38}$$

Inserting Eq. (38) in (36) and rearranging gives

$$P_{cp} = \frac{C_{p,a} W_{cp,out} T_{cp,in}}{\eta_{cp}} \left(\left(\frac{p_{cp,out}}{p_{cp,in}} \right)^{\frac{\gamma_a - 1}{\gamma_a}} - 1 \right). \tag{39}$$

Finally, it follows from Eq. (37) and (39) that

$$\tau_{cp} = \frac{C_{p,a} W_{cp,out} T_{cp,in}}{\omega_{cp} \eta_{cp}} \left(\left(\frac{p_{cp,out}}{p_{cp,in}} \right)^{\frac{\gamma_a - 1}{\gamma_a}} - 1 \right). \tag{40}$$

2.3.3. Experimental validation of the air supply model

For validating the air blower model, a test rig was set up as depicted in Fig. 4. The blower is driven by a brushless DC-motor. The blower speed ω_{cp}, the blower torque τ_{cp}, the motor current i_{cm}, the blower air mass flow $W_{cp,out}$, the outlet temperature $T_{cp,out}$, and the exit air pressure $p_{cp,out}$ are measured with the corresponding sensors shown in Fig. 4. Experiments are realized using a DSP system, where the input voltage to the blower motor v_{cm} is given and measured variables are observed and controlled. In order to vary the outlet pressure $p_{cp,out}$, a manually adjustable pressure regulating valve is used.

The applied blower from Ballard [11] belongs to the category of roots blowers and consists of two oval shaped lobe rotors inside the housing. One rotor is the driving rotor driven by the motor, while the other rotor is driven by a pair of gears with the same gear ratio. For this reason, both rotors rotate with the same speed [15]. First, the air enters the inlet side of the housing and between both rotors. As the rotors rotate towards the outlet side, the air is pushed against the housing of the blower. On the outlet side, the air is compressed up to the system pressure and forced out. During each rotation, four volumes are displaced. During the total working process, the air is only moved from the inlet side to the outlet side of the blower and no volume change of the air within the housing appears. One advantage of these kind of air blowers is that large amounts of air can be displaced in the

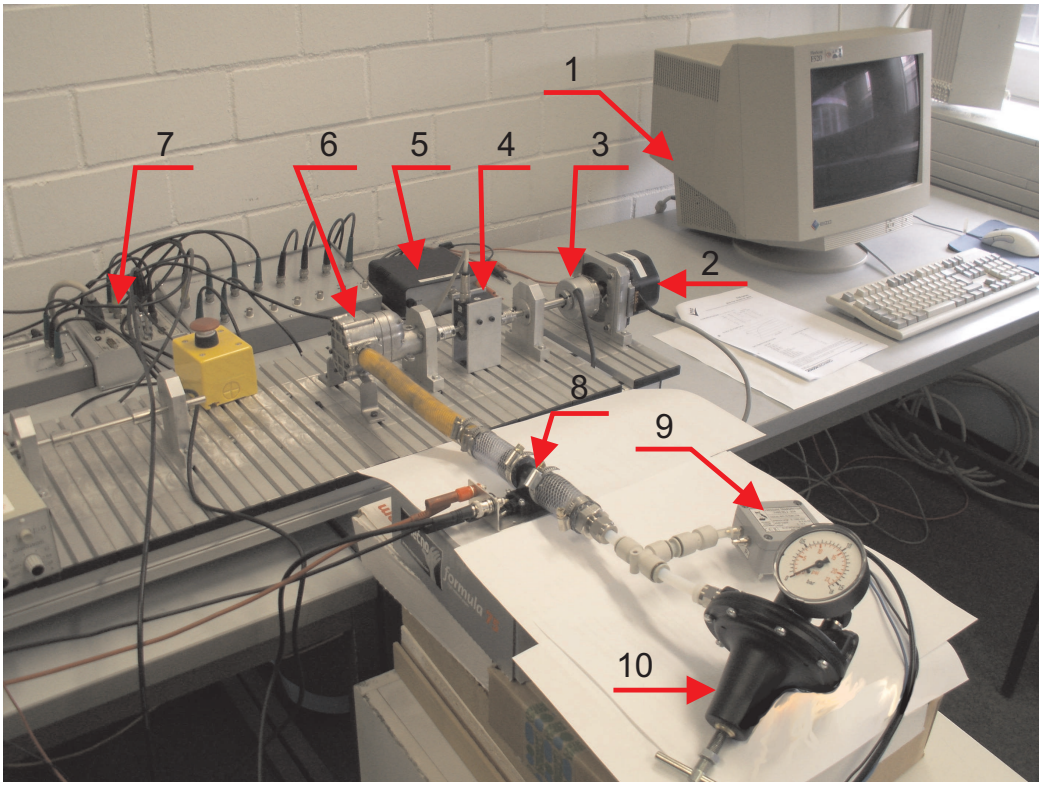

Figure 4: Test rig used for validation of the blower model at the Chair of Dynamics and Control, University of Duisburg-Essen.
1. Interface, 2. Brushless DC-motor, 3. Rotary speed sensor, 4. Torque sensor, 5. Current sensor, 6. Blower, 7. DSP system, 8. Air mass flow and temperature sensor, 9. Pressure sensor, 10. Pressure regulating valve

lower speed regions. However, a disadvantage of these kind of root blowers is that the thermal efficiency η_{cp} is low compared to e.g. centrifugal and screw blowers [15].

For validation, experiments are carried out in two steps: Firstly, the

blower is physically disconnected and the motor parameters are identified and separately validated. Secondly, the blower is connected and the blower parameters are identified based on measured data. During the experiment, the input voltage v_{cm} was incrementally increased from 2.4 V to 16.8 V with 2.4 V steps. The blower speed ω_{cp} increases respectively from 300 to 2100 rpm with an increment of 300 rpm. The outlet pressure $p_{cp,out}$ is manually adjusted with an increment of 10 mbar at each speed region.

The task of this step is to determine the constants of the static blower map a_i, b_i, d_i, e_i, and f_i for $i = 1, 2, 3$. According to the Eq. (25-30), the constants a_i and b_i describe the relation between the dimensionless parameter Ψ, the normalized mass flow rate Φ, and the Mach number Ma of the air entering the blower, while the constants d_i, e_i, and f_i denote the relation between the blower efficiency η_{cp}, the normalized mass flow rate Φ, and the Mach number. First, the parameters a_i, b_i, d_i, e_i, and f_i, the dimensionless variable Ψ, the normalized mass flow rate Φ, the Mach number, and the blower efficiency η_{cp} are determined. The dimensionless head parameter Ψ can be calculated with Eq. (28) and the Mach number Ma of the air entering the blower by Eq. (27). The reference values of the normalized mass flow rate Φ and the blower efficiency η_{cp} can be calculated with Eq. (22) and (40) to

$$\Phi_{ref} = \frac{4W_{cr}}{\rho_a \pi d_c^2 U_c} \tag{41}$$

and

$$\eta_{cp,ref} = \frac{C_{p,a} W_{cp,out} T_{in,cp}}{\omega_{cp} \tau_{cp}} \left(\left(\frac{p_{cp,out}}{p_{in,cp}} \right)^{\frac{\gamma_a - 1}{\gamma_a}} - 1 \right), \tag{42}$$

where the mass flow rate across the blower $W_{cp,out}$, the bower speed ω_{cp}, the torque to drive the blower τ_{cp}, and the pressure of the air leaving the blower

$p_{cp,out}$ are measured and the blower diameter d_c is known. In Eq. (41), the blower blade-tip speed U_c can be calculated with Eq. (23) and (24). The other parameters in Eq. (41) and (42) are assumed as constant. After determining the reference values of the normalized mass flow rate Φ_{ref} and the blower efficiency η_{cp}, the identification of the other parameters can be conducted. In order to identify the parameters $k_{i=1,2,3}$ in Eq. (25), a least square curve fitting approach is applied. The model error e_i is defined by

$$e_i = y_{ref}(x_i) - y(x_i), \quad i = 1, 2, \ldots, n, \tag{43}$$

where $y_{ref}(x_i)$ is the reference value from measurements at x_i and $y(x_i)$ the simulation result. The simulation results in this case are calculated with the simulated normalized blower flow rate from Eq. (25) with the input vector Ψ and the vector k_i of the model. The goal of the iteration algorithm is to minimize J_e, as the sum of the squared errors between reference and measurement, defined by

$$J_e = \sum_{i=1}^{n} e_i^2, \tag{44}$$

where n is the number of measurements. The goal of the identification process is to determine the optimal combination vector of the tuning parameters $k_{i,opt}$, so that J_e is minimized. During this process, the elements of the unknown parameter vector k_i have to be changed, until J_e reaches a minimum (or limit) as a break condition. Using the routine *fminsearch* in Matlab® an optimization process can be conducted. The approximation results of the factors are shown in Fig. 5 (a)-(c). The values of Φ as a function of Ψ and ω_{cp} calculated with the blower map model are graphically depicted in Fig. 6 (a). The blower efficiency η_{cp} is depicted in Fig. 6 (b).

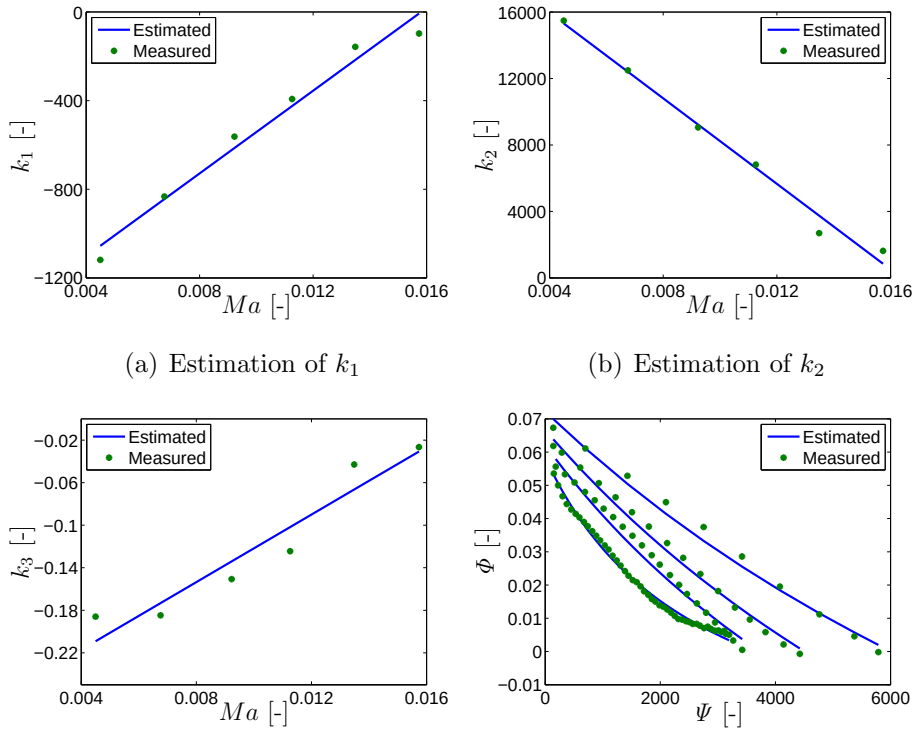

(a) Estimation of k_1

(b) Estimation of k_2

(c) Estimation of k_3

(d) Estimation between Φ and Ψ

Figure 5: Estimation of the parameters k_1, k_2, k_3, Φ, and Ψ

Finally, using the blower model and related identified parameters, an experiment is conducted to validate the model. The input blower voltage v_{cm} is changed with a series of voltage steps applied as input. The comparison between measured and simulated data is shown in Fig. 7. It is obvious that the dynamics of the blower speed (top figure), air flow (middle figure), and motor current (bottom figure) are well represented with the developed air supply system model.

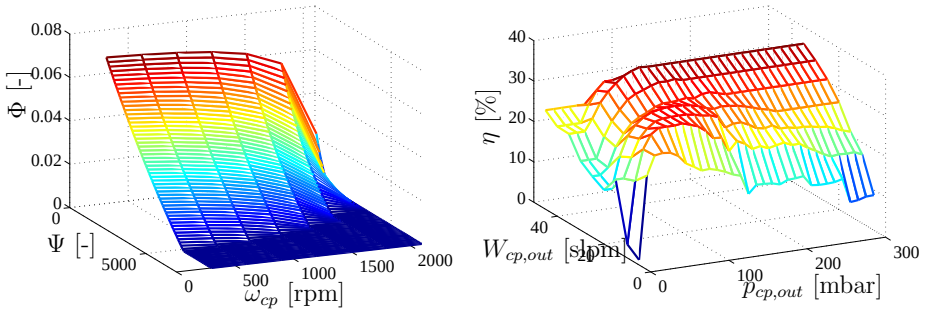

(a) Parameters Φ, Ψ, and ω_{cp} (b) Blower efficiency map

Figure 6: Left: Estimation of the parameters Φ and Ψ as a function of rotation speed. Right: Efficiency map of the blower

2.3.4. Linearization of the fuel cell model

For analytical examination, analysis of a fuel cell system, and for design of a suitable controller, it is helpful to linearize the nonlinear dynamical behavior of the fuel cell dynamics. In general, linearization of a nonlinear system makes it possible to apply conventional and powerful analyzing techniques such as stability, observability, and controllability examinations. A general explicit nonlinear system model can be presented as

$$\dot{x}(t) = f(x(t), u(t)), \quad x(0) = x_0 \tag{45}$$

$$y(t) = g(x(t), u(t)). \tag{46}$$

If the system model described with Eq. (45) and (46) is linearized at the operating point (x_{op}, u_{op}, y_{op}), the linearized system model (as state space model) can be written as

$$\delta\dot{x}(t) = \frac{\partial f(x(t), u(t))}{\partial x}|_{op}\delta x(t) + \frac{\partial f(x(t), u(t))}{\partial u}|_{op}\delta u(t), \tag{47}$$

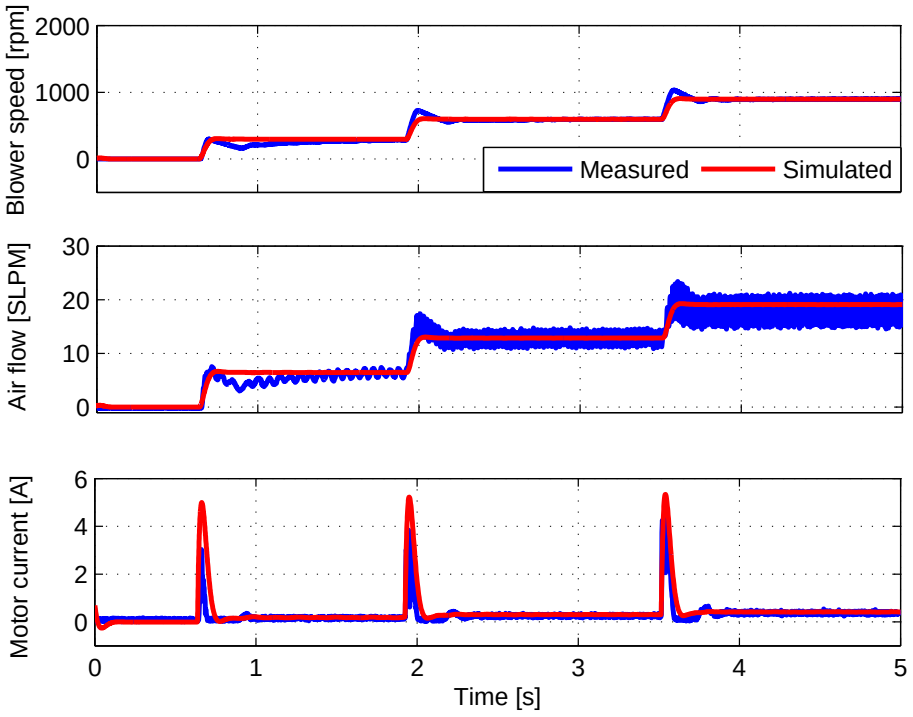

Figure 7: Validation of the dynamical behavior of the blower by comparison of the rotation speed, air flow, and motor current, using experimental results.

$$\delta y(t) = \frac{\partial g(x(t), u(t))}{\partial x}|_{op}\delta x(t) + \frac{\partial g(x(t), u(t))}{\partial u}|_{op}\delta u(t), \tag{48}$$

where the new linear state vector δx, the linear input vector δu, and the linear output vector δy are defined as

$$\delta x(t) = x(t) - x_{op}, \tag{49}$$

$$\delta u(t) = u(t) - u_{op}, \text{ and} \tag{50}$$

$$\delta y(t) = y(t) - y_{op}. \tag{51}$$

The linearized system model is written in state-space form as

$$\delta\dot{x}(t) = A\delta x(t) + B\delta u(t), \quad \delta x_0 = \delta x(0) \tag{52}$$

$$\delta y(t) = C\delta x(t) + D\delta u(t), \tag{53}$$

where A denotes the system matrix, B the input matrix, C the output matrix, and D the direct feed-through matrix. The current input i_{st} of the fuel cell system ranges between 0 and 60 A, so the linearization point is chosen at 30 A. The voltage input to the blower motor is set accordingly, the stationary values of the states that follow are defined as initial conditions. The system variables result to

$$\begin{aligned} x &= [m_{O_2} \quad m_{H_2} \quad m_{N_2} \quad m_{w,ca} \quad m_{w,an} \\ &\quad\ \ \omega_{cp} \quad p_{sm} \quad m_{sm} \quad p_{rm} \quad i_{cm}]^T, \\ u &= v_{cm} \\ w &= i_{st} \\ y &= \begin{bmatrix} v_{st} & W_{cp,out} & p_{sm} \end{bmatrix}^T, \qquad (54) \\ z &= \begin{bmatrix} \eta_{net} & \lambda_{O_2} \end{bmatrix}^T, \qquad (55) \end{aligned}$$

with x describing the state vector, u the input vector, w the disturbance vector, y the output vector, and z, as introduced, as a complementary output vector. The system is described by 10 state variables, 1 input variable, 1 disturbance variable, and 5 output variables including the performance variables η_{net} and λ_{O_2}.

3. Control of the fuel cell system

This section deals with the control of the fuel cell system. Hereby for principal investigations with respect to the comparison of the approaches

three different control approaches, i.e. static feed-forward, state-feedback, and newly developed gain-scheduling control are detailed. The advantage of the approaches chosen is the comparibly good applicability and simple implementation to real systems. All approaches are applied to a nonlinear fuel cell system model here for the first time. The results will allow the evaluation of the approaches. All control approaches mentioned use an underlying controller which is related to the hydrogen input mass flow $\dot{m}_{H_2}$ to minimize the pressure difference between anode and cathode.

For the implementation of the controllers to be compared it is assumed that the linearized system behavior is fully observable as well as fully controllable. Using Hautus or Gilbert criteria this can be done based on the developed linearized models. Due to the numerical structure of the models Kalman criteria checking the rank condition cannot be recommended.

The dynamical behavior of the fuel cell system is described by using a multiple-input-multiple-output (MIMO) state space representation as mentioned before. The inputs to the fuel cell system are

- the stack current i_{st},
- the blower input voltage v_{cm}, and
- the hydrogen input mass flow $\dot{m}_{H_2}$.

The outputs are

- the stack voltage v_{st} and
- the oxygen excess ratio λ_{O_2}.

As introduced in Section 2, the stack current appears here as disturbance. The blower motor input voltage v_{cm} is the input variable able to affect the fuel cells' dynamical behavior. The blower speed determines the oxygen input flow, so the oxygen excess ratio λ_{O_2} can directly be affected. Consequently, oxygen starvation can be avoided. Oxygen starvation occurs when the partial pressure of oxygen falls below a critical level at any possible location within the meander of the air stream in the cathode. This can occur during a sudden current step output. A severe oxygen starvation can cause a short cut and a hot spot on the surface of the membrane and cause irreversible damages to the membrane [16], so one of the control objectives is to avoid oxygen starvation and to keep the output oxygen excess ratio at an optimal level or to realize only dynamically smooth behaviors.

3.1. Efficiency constraints

The net efficiency of the fuel cell system can be calculated as

$$\eta_{net} = \frac{P_{net}}{W_{H_2,reacted}\Delta H_{h,H_2}} 100\%, \tag{56}$$

where P_{net} denotes the net power of the fuel cell system, $W_{H_2,reacted}$ the mass flow rate of the reacted hydrogen, and $\Delta H_{h,H_2}$ the higher heating value for hydrogen [9, 17]. The net power of the fuel cell system P_{net} is defined as

$$P_{net} = P_{st} - P_{cm}, \tag{57}$$

where P_{st} denotes the gross power of the fuel cell stack and P_{cm} the blower motor power provided from the fuel cell and accounts for some of the parasitic

losses. The variables are calculated as

$$P_{st} = v_{st} i_{st} \quad \text{and} \tag{58}$$

$$P_{cm} = v_{cm} i_{cm}, \tag{59}$$

where the fuel cell stack voltage v_{st} is calculated with Eq. (2), i_{st} and v_{cm} denote the current stack and the blower input voltage, which represent the system inputs of the fuel cell system model. The variable i_{cm} denotes the blower motor current. The excess oxygen ratio λ_{O_2} used as indicator of the net efficiency and the oxygen starvation is defined by

$$\lambda_{O_2} = \frac{W_{O_2,in}}{W_{O_2,reacted}}, \tag{60}$$

with $W_{O_2,in}$ denoting the mass flow rate of oxygen gas entering the cathode and $W_{O_2,reacted}$ representing the rate of reacted oxygen. For different fuel cell current loads, the relationship between the excess oxygen ratio λ_{O_2} and the fuel cell net efficiency η_{net} is depicted in Fig. 8. The optimal value for all currents is chosen as $\lambda_{O_2,opt}$ approximately 2, as marked in Fig. 8, which is assumed as an averaged maximum.

The mass flow rate of reacted oxygen $W_{O_2,reacted}$ is defined by

$$W_{O_2,reacted} = \frac{M_{O_2} n_{fc} i_{st}}{4F}, \tag{61}$$

with the molar mass of the oxygen M_{O_2}, the number of cells n_{fc}, and the Faraday number F. From Eq. (61), it becomes obvious that for a certain fuel cell system the mass flow rate of reacted oxygen only depends on the fuel cell current. Therefore the variable $W_{O_2,reacted}$ can not be influenced by controlling the fuel cell system. If the mass flow rate of oxygen gas entering

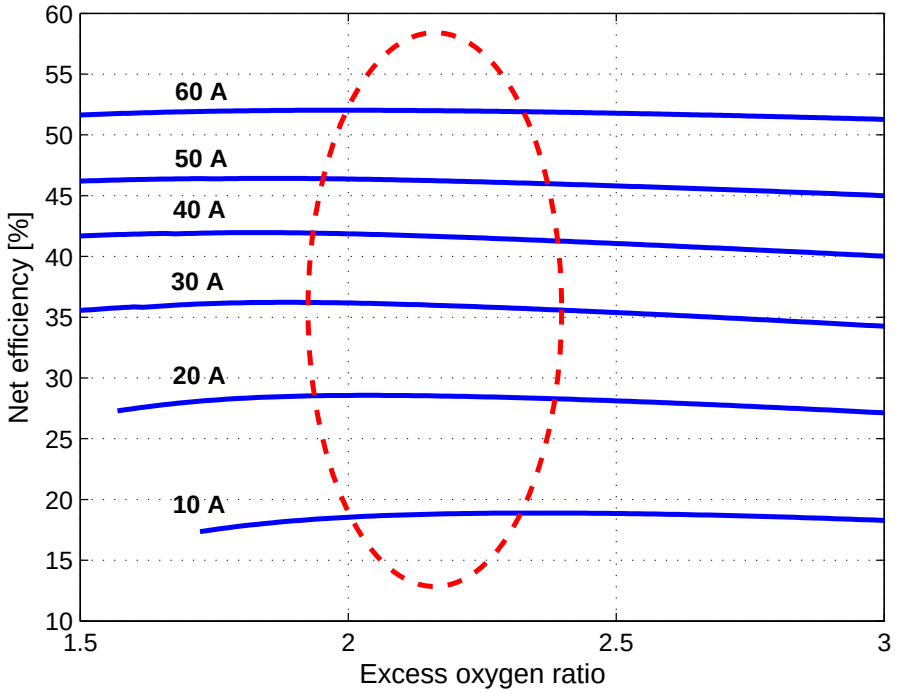

Figure 8: An optimal efficiency is achieved through different lambda values which can be controlled with the air-blower, which is depicted for different current steps.

the cathode $W_{O_2,in}$ during the increasing current draw is constant, the excess oxygen ratio λ_{O_2} decreases accordingly. As a consequence, the net efficiency of fuel cell η_{Net} decreases and oxygen starvation is imminent. In order to keep the excess oxygen ratio λ_{O_2} at an optimal value, the mass air flow rate has to be controlled. Inserting Eq. (57), (60), and (61) in (56) the efficiency η_{net} is given as

$$\eta_{net} = \frac{v_{st} 4F W_{O_2,in} - \lambda_{O_2} v_{cm} i_{cm} M_{O_2} n_{fc}}{W_{H_2,reacted} \Delta H_{h,H_2} M_{O_2} n_{fc} \lambda O_2}, \tag{62}$$

which is plotted in Fig. 8 as a function of λ_{O_2} for different stack load currents i_{st}.

3.2. Hydrogen valve control

The hydrogen of the considered system supplied from a high-pressure tank comes with a flow rate controlled by a valve. This gives a relatively rapid adjustment of the flow rate and anode pressure. This valve control is applied independently from the controller systems described in section 3. The control variable is the anode pressure and as reference value the cathode pressure is used. This means, the control goal is to minimize the pressure difference between anode and cathode, therefore a PI-controller is used. Since the output control value is the anode pressure p_{an} and the input variable is the anode inlet flow $W_{an,in}$, the equation (without interfering from any disturbances) is given by

$$p_{H_2} = \frac{R_{H_2} T_{fc}}{V_{an}} m_{H_2}, \tag{63}$$

here m_{H2} is calculated as the integral of the difference between injected and consumed hydrogen flows by

$$m_{H_2} = \int_0^t (W_{H_2,in} - W_{H_2,reacted}) dt. \tag{64}$$

The variable $W_{H2,reacted}$ is directly considered as a disturbance through the output current according to

$$W_{H_2,reacted} = M_{H_2} \frac{n i_{st}}{2F}. \tag{65}$$

Calculating the transfer function (as shown in Fig. 9) from the consumed hydrogen $W_{H_2,reacted}$ gives

$$G_{p_{H_2},W_{H_2,reacted}} = -\frac{R_{H_2} T_{fc}}{s(V_{an} + V_{an} K)}, \tag{66}$$

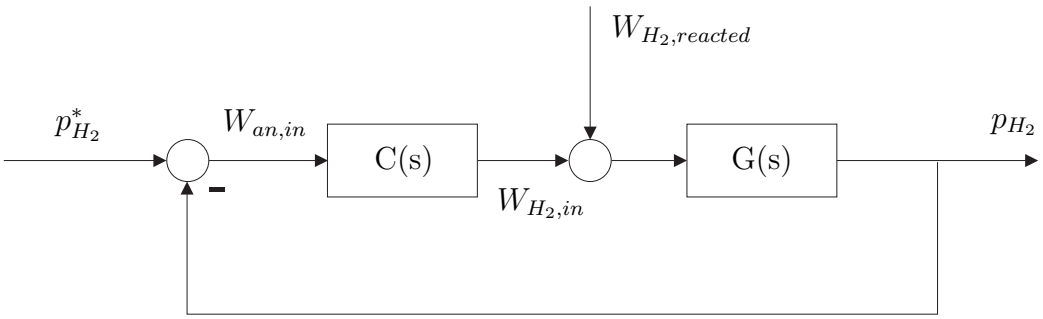

Figure 9: Flow diagram of the hydrogen valve control loop

whereby the transfer function using a PI-controller with K as proportional gain and T_I as design parameter yields

$$\begin{aligned} P_{H_2}(s) = \frac{KR_{H_2}T_{fc}(s+T_I)}{Vs^2+KRTs+KRTT_I}R(s) - \\ - \frac{sRT}{Vs^2+KRTs+KRTT_I}W_{H_2,reacted}(s). \end{aligned} \tag{67}$$

Examining the final values for $t \to \infty$ using the final-value-theorem, the final value of a given reference step gives

$$\lim_{s\to 0} \; -s\frac{1}{s}\frac{KR_{H_2}T_{fc}(s+T_I)}{Vs^2+KRTs+KRTT_I} = 1. \tag{68}$$

For a disturbance step function the final value results to

$$\lim_{s\to 0} \; -s\frac{1}{s}\frac{sR_{H_2}T_{fc}}{Vs^2+KRTs+KRTT_I} = 0, \tag{69}$$

which includes that any disturbances are rejected, using only a P-controller as suggested in [2]. The related transfer function results to

$$P_{H_2}(s) = \frac{KR_{H_2}T_{fc}}{Vs+KRT}R(s) - \frac{RT}{Vs+KRT}W_{H_2,reacted}(s). \tag{70}$$

Applying the final-value-theorem to examine the stationary values for an input step function for the reference signal gives

$$\lim_{s\to 0}\ s\frac{1}{s}\frac{KR_{H_2}T_{fc}}{V_{an}s + KR_{H_2}T_{fc}} = 1, \tag{71}$$

and for the disturbance

$$\lim_{s\to 0}\ -s\frac{1}{s}\frac{R_{H_2}T_{fc}}{V_{an}s + KR_{H_2}T_{fc}} = -\frac{1}{K}. \tag{72}$$

As expected, the disturbance can not be accommodated using P-control. Due to the stationary behavior and the integral behavior of the system it can not be recommended to use a P-control due to this stationary error as mentioned in [2]. Instead, a PI-control can be used in order to eliminate the stationary error completely as depicted in Fig. 10. The transfer function from the reference value to the output results to

$$G_{r,p_{H_2}}(s) = R_{H_2}T_{fc}K\frac{s + T_I}{V_{an}s^2 + R_{H_2}T_{fc}Ks + R_{H_2}T_{fc}KT_I}. \tag{73}$$

Depending on the parameters oscillations of the resulting PDT_2-system may occur. Using root-locus analysis, the integral coefficient T_I determines the bandwidth of the closed system so the proportional coefficient K canbe defined to avoid any kind of oscillations.

3.3. Three approaches to control oxygen excess ratio

As mentioned, three control approaches of the fuel cell system are implemented and compared to each other. Hereby the trajectory of the oxygen excess ratio λ_{O_2} is applied to evaluate the performance of the parameters.

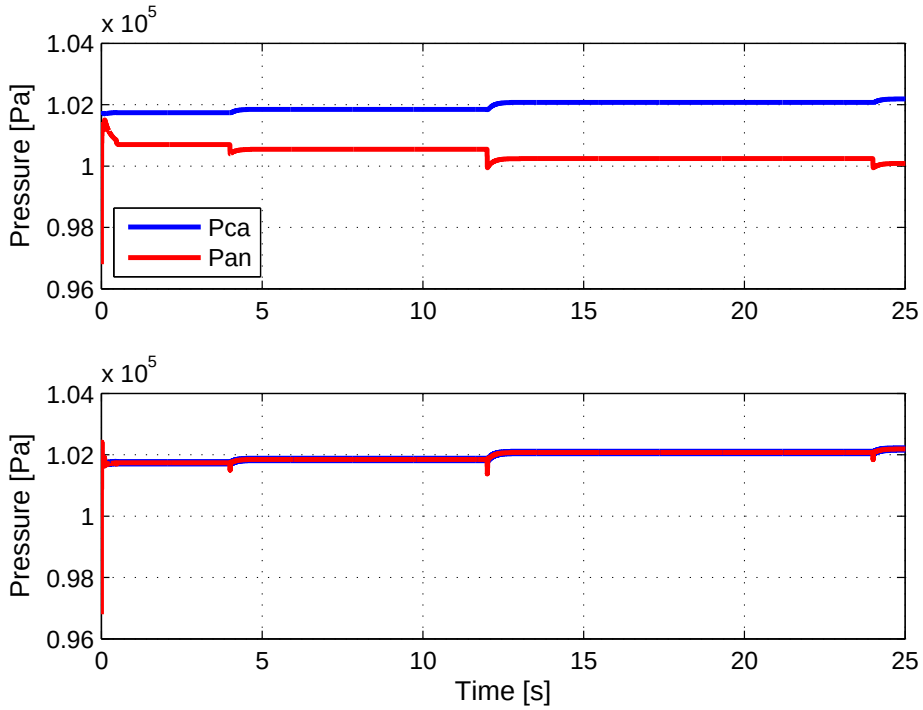

Figure 10: Cathode and anode pressures for a P- (top) respectively PI-controller (bottom) for the hydrogen valve

3.3.1. Control approach I: Static Feed-Forward control

A classical way to control a fuel cell system is using an open-loop feed-forward control approach [2]. This method only requires the measurement of the current load of the fuel cell system, the knowledge of the system behavior (if the control input is previously calculated or optimized). The control approach is easy to be implemented and therefore should not be detailed here. The input signal to the system, i.e. the input voltage to the blower motor v_{cm}, can be represented with a look-up table, for example based

on the data as given in Fig. 8. As result, the input voltage of the electromotor drives the blower at its optimal working point for each current load i_{st} of the fuel cell system. The implementation of the look-up table in the feed-forward concept is briefly depicted in Fig. 11.

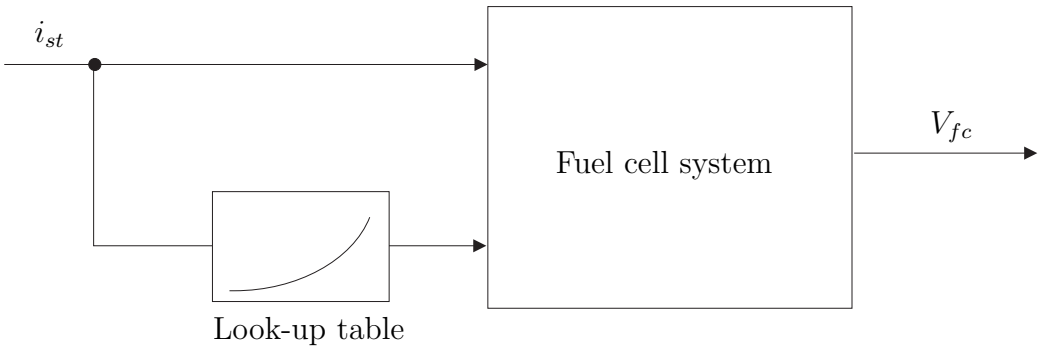

Figure 11: Control schedule of the static feed-forward controller

3.3.2. Control approach II: Optimal control

A Linear Quadratic Regulator (LQR) optimal control is applied to design a state-feedback controller. As introduced in the previous sections, the target of the control is to minimize the response of the excess oxygen ratio λ_{O_2} from its reference. In the linearized model, this variable is denoted by δz_2 using the relation

$$z_2 = \begin{bmatrix} 0 & 1 \end{bmatrix} \; z = \lambda_{O_2}. \tag{74}$$

The LQR-related cost function $\tilde{J}$ is defined by

$$\tilde{J} = \int_0^\infty \left(\delta z_2^T Q_z \delta z_2 + \delta u^T R \delta u \right) dt, \tag{75}$$

using the weighting matrices Q_z and R of the performance variable δz_2 and the input δu respectively. In order to follow the desired value of the excess

oxygen ratio λ_{O_2}, an additional state q has to be defined. A direct relation between desired $\lambda_{O_2,d}$ and the desired mass flow rate across the blower $W_{cp,d}$ is defined by [2]

$$W_{cp,d} = \left(1 + \frac{M_v}{M_a} \frac{p_{sat}(T_{in,cp})}{p_{in,cp} - p_{sat}(T_{in,cp})}\right) \frac{M_{O_2} n}{x_{O_2} 4F} i_{st} \lambda_{O_2,d}, \tag{76}$$

with M_v, M_a, and M_{O_2} as the molar masses of vapor, dry air, and oxygen respectively; $p_{sat}(T_{in,cp})$ denotes the vapor saturation pressure at temperature $T_{in,cp}$, and x_{O_2} denotes the oxygen mass fraction in dry air. Using this desired value, an additional state q is defined by

$$\dot{q} = W_{cp,d} - W_{cp,out} = W_{cp,d} - C_{y_2} \delta x, \tag{77}$$

where the mass flow rate across the blower $W_{cp,out}$ in case of a real application can be measured. Using the LQR approach design, in order to minimize the additional state q, the cost function $\tilde{\tilde{J}}$ has to be transformed to

$$\tilde{\tilde{J}} = \int_0^\infty \left(\delta z_2^T Q_z \delta z_2 + q^T Q_q q + \delta u^T R \delta u\right) dt, \tag{78}$$

with the weighting function Q_q for the state q. Using the assumption

$$\delta z_2 = C_{z_2} \delta x, \tag{79}$$

the cost function becomes

$$\tilde{\tilde{J}} = \int_0^\infty \left(\delta \hat{x}^T \hat{Q} \delta \hat{x} + \delta u^T R \delta u\right) dt, \tag{80}$$

where the weighting matrix $\hat{Q}$ is defined as

$$\hat{Q} = \begin{bmatrix} C_{z_2}^T Q_z C_{z_2} & 0 \\ 0 & Q_q \end{bmatrix} \tag{81}$$

and the new state vector $\hat{x}$ is defined as

$$\hat{x} = \begin{bmatrix} \delta x \\ q \end{bmatrix}. \tag{82}$$

According to the principle of the LQR optimal controller, the control input is

$$\delta u = -K_{opt}\delta\hat{x}, \tag{83}$$

with K_{opt} as the controller gain matrix calculated from

$$K_{opt} = R^{-1}\hat{B}_u P, \tag{84}$$

where $\hat{B}_u$ denotes the input matrix of the system describing the additional state q and P denotes the solution matrix of the algebraic Riccati equation. The state-space model of the system with the additional state q result to

$$\delta\dot{\hat{x}} = \hat{A}\delta\hat{x} + \hat{B}_{u_1}\delta u_1 + \hat{B}_{u_2}\delta u_2 \tag{85}$$

with the compressor motor voltage u_1 and the stack current u_2 used as system inputs. The relating matrices are given by

$$\hat{A} = \begin{bmatrix} A & 0 \\ A_q & 0 \end{bmatrix}, \quad \hat{B}_u = \begin{bmatrix} B_u \\ 0 \end{bmatrix}, \quad \hat{B}_w = \begin{bmatrix} B_w \\ B_q \end{bmatrix}. \tag{86}$$

The matrix A_q can be calculated according to Eq. (77) by

$$A_q = -C_{y_2}, \tag{87}$$

the matrix B_q according to Eq. (76) by

$$B_q = \left(1 + \frac{M_v}{M_a}\frac{p_{sat}(T_{in,cp})}{p_{in,cp} - p_{sat}(T_{in,cp})}\right)\frac{M_{O_2} n}{x_{O_2} 4F}\lambda_{O_2,d}. \tag{88}$$

Due to the structure of A_q (and modelled singular eigenvalues) controllability of the entire system resp. asymptotical zero dynamics has to be assumed for successful realization.

3.3.3. Control approach III: Gain-Scheduling control

Since fuel cells show strong nonlinear behavior over their operating range, the possibility of implementing nonlinear control approaches can be desired. For the state-feedback method, the system is linearized at a single working point and the linear controller is applied. For strong nonlinear systems like the dynamical behavior of fuel cells, this can be insufficient from a performance point of view as it can be seen from the results presented in the sequel. The same discussion appears with respect to the stability of the system. Using gain-scheduling control, it may be possible to apply related controllers at each working point based on linearized system models of several nominal working points. Thereafter, different controllers can be interpolated between each other and implemented on the fuel cell system within the whole operating range. Due to the unknown overall nonlinear characteristics of the system this problem also appears with other approaches so final tests have to be applied for experimental checking the behavior. The linearization points for the gain-scheduling controller for this fuel cell system are chosen to i_{st} = 10, 20, 30, 40, 50, and 60 A. Of course, from this multi-model approach obviously a guaranteed statement about the overall stability can not be concluded, nevertheless this strategy allows in combination with related practical experiments conclusions with respect to BIBO-stability of the used operating parameters. Alternatively, the stability check can be done experimentally, which will be the easiest way to be realized. A strategy to check stability numerically is shown in [18]. The developed approach covers the whole working range of the considered system. The distance between the linearization points can be chosen suitably to realize satisfying results. The gain-scheduled linearized

system model is represented in state-space form with

$$\delta\dot{x}(t) = A_i\delta x(t) + B_i\delta u(t), \quad \delta x_0 = \delta x(0) \tag{89}$$

$$\delta y(t) = C_i\delta x(t) + D_i\delta u(t). \tag{90}$$

Optimal controller gains are calculated for each working point $K_{opt,i}$ according to Eq. (84). An interpolation based on a polynomial approach is applied to determine the controller matrix. In Fig. 12, the interpolation between the matrix-elements of the gain-scheduled optimal controller matrix $K_{opt,i}$ is depicted. It can be seen that the elements are smoothly changing their values between the working points to be linearized. Using the strategy shown in [18] it is possible to realize the gain-scheduling controller and to implement the controller at the same time allowing a fast and smooth switching between the linearization points.

4. Results

The three control approaches are compared by simulations. All three approaches us the underlying hydrogen valve controller as introduced in Section 3.2. As input signal a series of current step functions within the operating range of the fuel cell is applied, as depicted in Fig. 13. The input signal is chosen in the way that it includes currents at the linearization points as well as intermediate currents to show the control performance for both cases.

The results of the three control approaches are shown in Fig. 14. As desired value of the excess oxygen ratio the value $\lambda_{O_2} = 2$ is chosen.

The state-feedback controller gives a stationary error in working points different from the assumed linearization point (here realized at approx. 20 s with of 30 A).

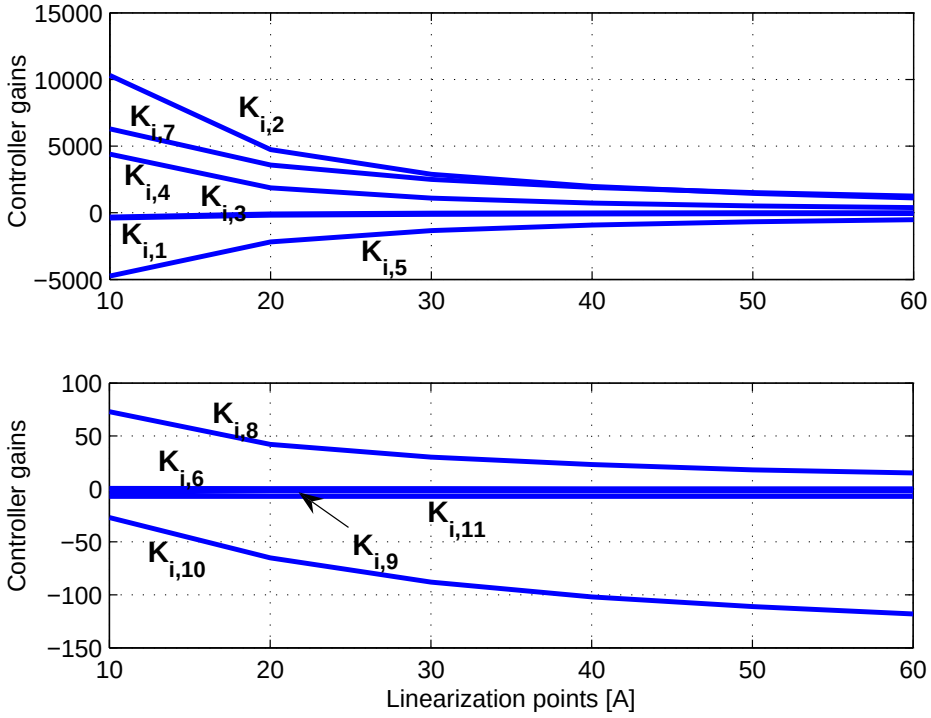

Figure 12: The gain-scheduling controller is interpolated between the linearization working points. Top: Large value gains. Bottom: Small value gains

Zooming at a current step outside the linearization point, e.g. at 10 s, the results are depicted in Fig. 15. It is shown that the state-feedback and the gain-scheduling control methods are advantageous in relation to the static feed-forward method in keeping the excess oxygen ratio at an optimal point and preventing oxygen starvation.

Depicted results are shown in Fig. 16 zooming Fig. 14 at the linearization point. The state-feedback and gain-scheduling controllers show almost

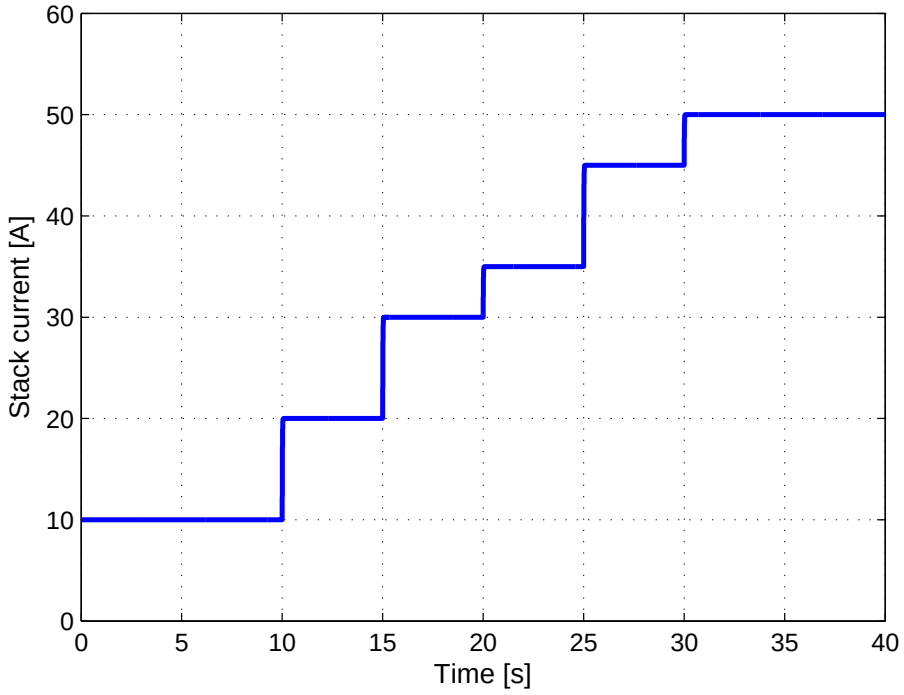

Figure 13: Input current variable used as input for comparing the control approaches

similar results while the static feed-forward controller shows slower response to recover the optimal value of the oxygen excess ratio.

5. Summary and outlook

In this paper, models of the static and dynamic behavior of the components and the overall system behavior of a fuel cell system including an air blower are presented and validated to real system behavior. As underlying controller for the anode pressure three typical and practically easy to ap-

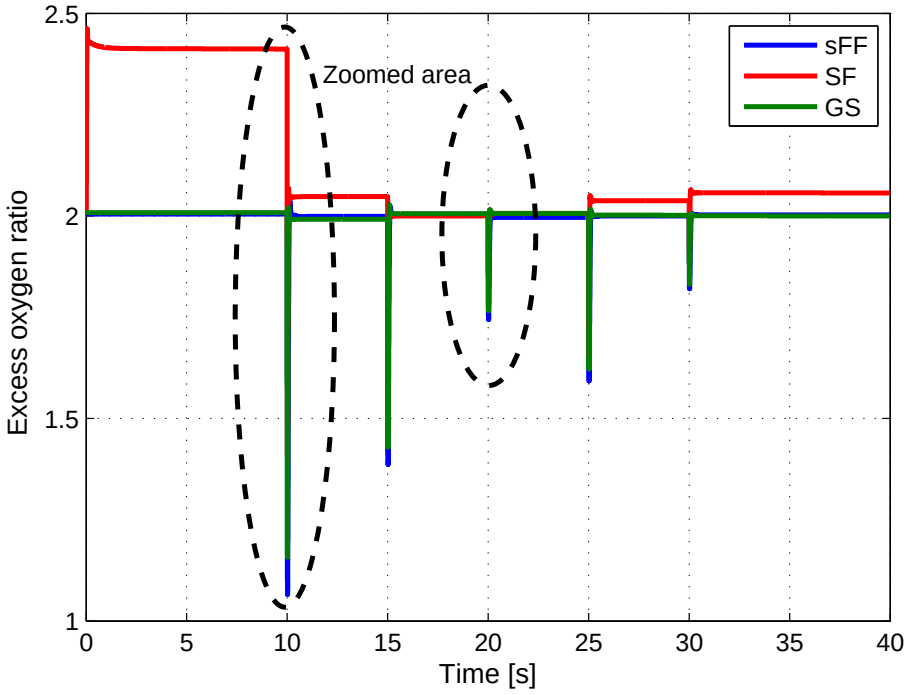

Figure 14: Comparison of the static feed-forward (sFF), state feedback (SF), and gain-scheduling control (GS) applied for a nonlinear fuel cell model

ply control design approaches are implemented an compared to each other. The first one proposed is a PI-controller for the hydrogen valve. The implementation of an integral part eliminates the stationary error that usually occurs with a P-controller which is proposed in the literature. Based on the developed models, two conventional controllers , a static feed-forward controller and a state-feedback controller, are applied and a new controller (Gain scheduling) is developed; all approaches are compared. Besides some

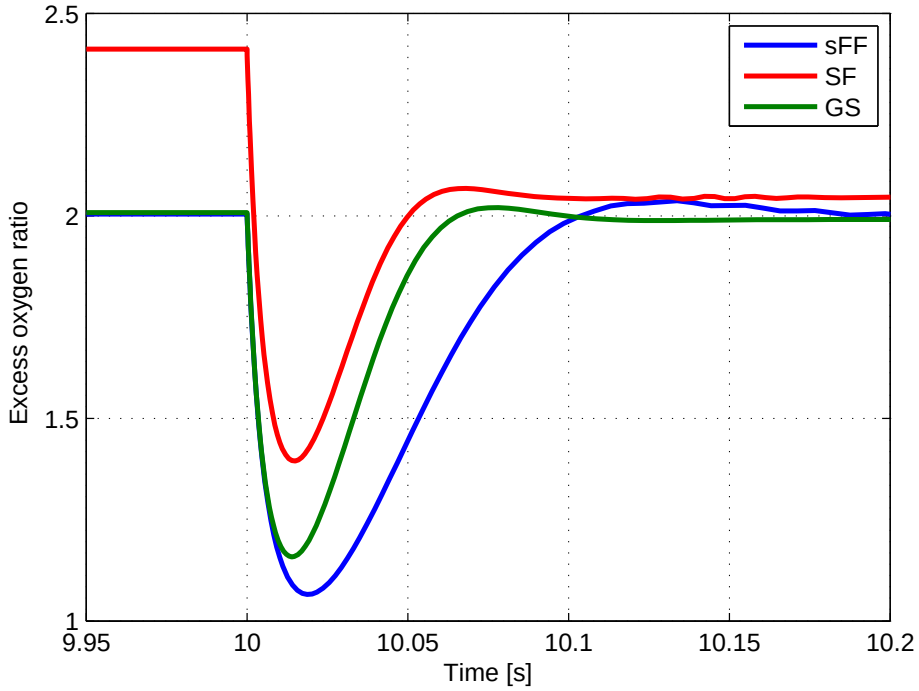

Figure 15: Zoomed area for a step current output for static feed-forward (sFF), state feedback (SF), and gain-scheduling control (GS)

principal aspects (e.g. stationary error (SF)), the dynamical behavior of the approaches are comparable, in detail the results are different. It can shown that the gain-scheduling controller shows better results than static feed-forward and state-feedback over the entire working range of the fuel cell system. The state-feedback controller shows good performance in preventing oxygen starvation, but has a stationary error in working points outside the linearization point. This can lead to a decrease in the efficiency of the fuel cell system, when used in an arbitrary application with a dynamic load pro-

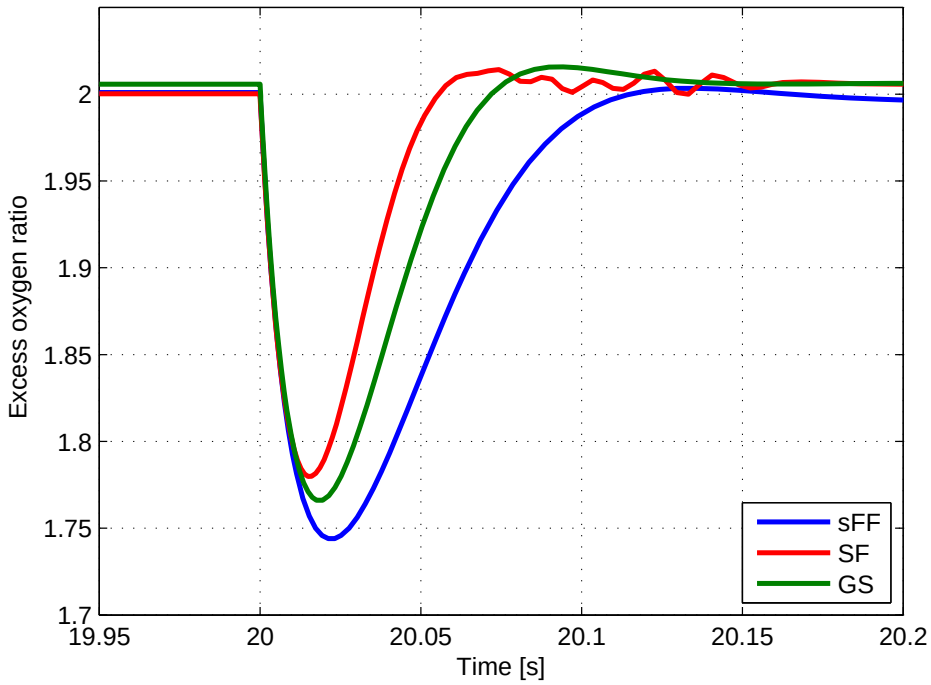

Figure 16: Zoomed area around the working linearization point for a step current output for static feed-forward (sFF), state feedback (SF), and gain-scheduling control (GS)

file [19]. The gain-scheduling controller seems to be well suited for this kind of applications. The corresponding models of the fuel cell system including the air blower are modeled and validated.

In future the developed gain-scheduling control approach will be implemented on the presented real fuel cell system. Dependent on the type and structure of the fuel cell system the implementation of observer structures might be necessary. For the related realization an investigation of the ob-

servability of the overall system can additionally be conducted in order to realize state-feedback control based on the existing sensors of the system or by the use of suitable observers as described e. g. in [20]. Additionally the stability assumed for the transition between the working points has to be proven as described in [18].

The choice of the weighting matrices Q and R for the state feedback controller described here will also have an influence on the controller performance. Further improment might be possible with the adaption of them e.g. dependent on the current load profile. Furthermore, with the assumption of a previously known load profile or the application of a prediction approach of the load profile the application of a Model Predictive Controller will be an alternative option to realize the control goal.

References

[1] J. Zhang, G. Liu, W. Yu, M. Ouyanga, Adaptive control of the airflow of a PEM Fuel Cell System, Journal of Power Sources 179 (2) (2008) 649–659.

[2] J. T. Pukrushpan, A. G. Stefanopolou, H. Peng, Control of Fuel Cell Power Systems: Principles, Modeling, Analysis, and Feedback Design, Springer-Verlag, London Limited, 2004.

[3] M. Grujicic, K. M. Chittajallu, E. H. Law, P. J. T., Model based control strategies in the dynamic interaction of air supply and fuel cell, Proceedings of the Institution of Mechanical Engineers, Part A: Journal of Power and Energy 218 (7) (2004) 487–499.

[4] W. K. Na, B. Gou, B. Diong, Nonlinear control of pem fuel cells by exact linearization, IEEE Transactions On Industry Applications 43 (6) (2007) 1426–1433.

[5] M. A. Danzer, J. Wilheim, H. Aschemann, E. P. Hofer, Model-based control of cathode pressure and oxygen excess ratio of a PEM fuel cell system, Journal of Power Sources 176 (2) (2008) 515–522.

[6] S. Pierfederici, P. Thoumthong, P. Sethakul, S. Sikkabut, B. Davat, Differential flatness-based control for fuel cell hybrid power source, in: Proceedings of the 1st International Conference on Technical Educaton, 2010.

[7] D. J. Leith, W. E. Leithhead, Survey of gain-scheduling analysis and design, International Journal of Control 73 (11) (2000) 1001–1025.

[8] Zentrum für BrennstoffzellenTechnik ZBT GmbH, Carl-Benz-Strae 20, 47057 Duisburg, Deutschland.
URL `www.zbt-duisburg.de (16-11 2009)`

[9] J. Larminie, A. Dicks, Fuel Cell Systems Explained, John Wiley & Sons, Ltd., Baffins Lane, Chichester, West Sussex, U.K., 2000.

[10] T. E. Springer, T. A. Zawodzinski, S. Gottesfeld, Polymer Electrolyte Fuel Cell Model, Journal of the Electrochemical Society 138 (8) (1991) 2334–2342.

[11] Ballard Power Systems Inc., 9000 Glenlyon Parkway, Burnaby, BC, V5J 5J8 Canada.
URL `www.ballard.com (16-11 2009)`

[12] J. M. Cunningham, M. A. Hoffman, R. M. Moore, D. J. Friedman, Requirements for a flexible and realistic air supply model for incorporation into a fuel cell vehicle (fcv) system simulation, Tech. Rep. 1999-01-2912, SAE (1999).

[13] P. Moraal, I. Kolmanovsky, Turbocharger modeling for automotive control, in: International Congress & Exposition, 1999.

[14] M. J. Moran, H. N. Shapiro, Fundamentals of engineering thermodynamics : [Sl units], 5th Edition, Wiley, Chichester, U.K., 2007.

[15] A. Kapur, R. Malhotra, U. Dutta, Roots blowers: Understanding twin lobe operation, Chemical Engineering World 37 (7) (2002) 78–80.

[16] A. Vahidi, A. Stefanopoulou, H. Peng, Model predictive control for starvation prevention in a hybrid fuel cell system, American Control Conference, 2004. Proceedings of the 2004.

[17] H. D. Bähr, S. Kabelac, Thermodynamik, Springer-Verlag Berlin, 2006.

[18] Y. Al-Sweiti, D. Söffker, Modeling and control of an elastic ship-mounted crane using variable gain model-based controller, Journal of Vibration and Control 13 (5) (2007) 657–685.

[19] M. Uzunoglu, M. S. Alam, Dynamic modeling, design and simulation of a pem fuel cell/ultra-capacitor hybrid system for vehicular applications, Energy Conversion and Management 48 (2007) 1544–1553.

[20] D. Söffker, T.-J. Yu, P. Müller, State Estimation of Dynamical Systems

with Nonlinearities by using Proportional-Integral Observer, International Journal of System Science 26 (9) (1995) 1571–1582.